Nanoscale

Patterning and doping of Transition Metals in Tungsten Dichalcogenides

Journal:	*Nanoscale*
Manuscript ID	NR-ART-08-2022-004677.R1
Article Type:	Paper
Date Submitted by the Author:	21-Oct-2022

Complete List of Authors:	Lin, Yung-Chang; National Institute of Advanced Industrial Science and Technology (AIST), Chang, Yao-Pang; National Tsing Hua University Chen, Kai-Wen; National Synchrotron Radiation Research Center Lee, Tai-Ting; National Tsing Hua University Hsiao, Bo-Jiun; National Tsing Hua University Tsai, Tsung-Han; National Tsing Hua University Yang, Yueh-Chiang; National Tsing Hua University Lin, Kuang-I; National Cheng Kung University, Core Facility Center Suenaga, Kazu; Osaka University, The Institute of Scientific and Industrial Research (ISIR-SANKEN) Chen, Chia-Hao; National Synchrotron Radiation Research Center, Chiu, Po Wen; National Tsing Hua University, Electrical Engineering

Patterning and doping of Transition Metals in Tungsten Dichalcogenides

Yung-Chang Lin[1], Yao-Pang Chang[2], Kai-Wen Chen[3], Tai-Ting Lee[2], Bo-Jiun Hsiao[2], Tsung-Han Tsai[2], Yueh-Chiang Yang[2], Kuang-I Lin[4], Kazu Suenaga[1,5], Chia-Hao Chen[3], and Po-Wen Chiu*[2,6]

[1]Nanomaterials Research Institute, National Institute of Advanced Industrial Science and Technology (AIST), Tsukuba 305-8565, Japan
[2]Department of Electrical Engineering, National Tsing Hua University, Hsinchu 30013, Taiwan
[3]National Synchrotron Radiation Research Center, Hsinchu 30076, Taiwan
[4]Center for Micro/Nano Science and Technology, National Cheng Kung University, Tainan 70101, Taiwan
[5]The Institute of Scientific and Industrial Research (ISIR-SANKEN), Osaka University, Osaka 567-0047, Japan
[6]Institute of Atomic and Molecular Sciences, Academia Sinica, Taipei, 10617, Taiwan

*Correspondence to: pwchiu@ee.nthu.edu.tw

ABSTRACT

Substitutional transition metal doping in two-dimensional (2D) layered dichalcogenides is of fundamental importance in manipulating their electrical, excitonic, magnetic, and catalytic properties through the variation of *d*-electron population. Yet, most doping strategies are spatially global, with dopants embedded concurrently during the synthesis. Here, we report an area-selective doping scheme for W-based dichalcogenide single layers, in which pre-patterned graphene is used as a reaction mask in high-temperature substitution of W sublattice. The chemical inertness of the thin graphene layer can effectively differentiate the spatial doping reaction, allowing for local manipulation of the host 2D materials. Using graphene as a mask is also beneficial in the sense that it also acts as an insertion layer between the contact metal and the doped channel, capable of depinning the Fermi level for low contact resistivity. Tracing the doping by means of chalcogen labelling, deliberate Cr embedment is found to become energetically favorable at the presence of chalcogen deficiency, assisting the substitution of W sublattice in the devised chemical vapor doping scheme. Atomic characterization using scanning transmission electron microscopy (STEM) shows that the dopant concentration is controllable and varies linearly

with the reaction time in the current doping approach. With the same method, other transition metal atoms such as Mo, V, and Fe can also be doped in the patterned area.

KEYWORDS

2D materials, TMD, doping, patterning, substitution, transition metals

Semiconductor doping via mass-selective ion implantation is a successful technique to acquire desirable electrical and optical properties in modern silicon technologies. Using pre-patterned photoresist as a mask, this approach offers a site- and depth-specific embedment of doping impurities. However, this technique is not applicable to materials with atom-scale thickness, such as graphene and transition metal dichalcogenides (TMDs).[1] Embedment of foreign impurities using ion bombardment is liable to smash the structural integrity of such semiconductors that may not be recovered by post-doping annealing.[2–4] To comply with the nature of finite thickness, substitutional doping in TMD materials is generally carried out during the crystal growth.[5–11] In this case, lattice substitution by transition metal (TM) impurities is spatially global.[12] As such, a doping methodology that can be area-selective and controllable over the doping level is highly desirable and has become one of the most pressing barriers for the development of advanced electronics based on TMD semiconductors. Recently, nanopatterning technology has been greatly utilized for defect engineering, phase manipulation, atomic modification, and post-synthesis of lateral heterostructures.[13,14] Besides, graphene has also been demonstrated as a nice confinement to grow TMD locally.[15–17] However, up-to-date, doping TMDs at the desired pattern areas remain elusive.

Here, we show a doping scheme for single-layer tungsten dichalcogenides, which allows area-selective substitution of TM sublattice using chemical vapor deposition (CVD) while retaining their crystalline integrity. The doping is proceeded via an “open-replace-close” (ORC) reaction, resembling the formation of lateral heterostructure. We exemplify using Cr as a dopant for single-layer WSe_2 in this work. The area-specific reaction is realized using single-layer graphene as a mask, under which the host semiconductor remains pristine and intact, whereas the exposed areas proceed the ORC reactions. The advantage of using graphene as a mask lies in the following three aspects: (1) graphene

shows great chemical and thermal stability under the ORC doping conditions, and the Cr dopants cannot penetrate through the masked area. Based on experimental findings, a high-quality single-layer graphene was found to be sufficient for masking the doping reaction. (2) In contrast to inert graphene, the conventional masking materials such as Si_3N_4, SiO_2, and Al_2O_3 will participate the ORC doping process, and a large amount of metal atoms will be dissolved into these masking oxides at the high reaction temperature,[18] alternating the oxide chemistry for post-doping removal. Removal of these masking oxides requires the usage of stronger acids or alkalis, which causes excess defects in TMD. (3) Using graphene as a mask is also beneficial for further electronic applications in the sense that it can also act as an insertion layer between the contact metal and the doped channel, capable of depinning the Fermi level for low contact resistivity.[19,20] As a result, it is unnecessary to remove the graphene layer after the ORC doping process.

Results

Figure 1 shows the schematics of the ORC substitution process for WSe_2 doped with Cr (Figure 1a), along with the CVD setup (Figure 1b) and temperature versus time reaction diagram (Figure 1c). In this example, the ORC reaction is labelled by means of Se substitution by S in the unmasked area. The ORC doping method consists of three reaction phases. Phase I is the hydrogen-assisted Se desorption by following the chemical equation: $WSe_2(s) + H_2(g) \rightarrow WSe_{2-x}(s) + H_2Se(g)$. The reaction starts with heating the sample up to a fixed temperature of 715 °C, at which Se atoms can slowly escape from the lattice with the aid of hydrogen, forming gaseous H_2Se and leaving massive Se vacancies (V_{Se}) in the host WSe_2. Phase II is the defect-assisted interdiffusion. Herein, the dopant source, chromium (III) oxide, is placed in the close vicinity of the sample and heated up to the reaction temperature simultaneously. The chromium oxide can be reduced at the elevated temperature and brought to the surface of WSe_{2-x}. The reaction of Cr_2O_3 and H_2 at high temperature should follow the chemical equation: $Cr_2O_3 + 3H_2 \rightarrow 2Cr + 3H_2O$, as a result, the Cr species should arrive to the WSe_2 surface in the form of adatoms. The Se vacancies V_{Se} provide low-energy trap sites for Cr adsorption. Atomic characterization using scanning transmission electron microscopy (STEM) and density functional theory calculations show that they are bound to form a low-energy Cr-V_{Se} complex.[21] At the same

reaction temperature, Cr atoms can be embedded into the lattice and interdiffuse with W atoms, forming Cr-doped WSe_{2-x} (Cr:WSe_{2-x}) (i.e., Cr + WSe_{2-x}(s) -> Cr:WSe_{2-x}(s)). We note here that the phases I and II are dynamic reaction processes taking place simultaneously, and the flow rate of hydrogen plays an important role for doping. An optimal Ar and H_2 flow rates in our reaction chamber are 200 and 5 sccm. Over reaction with hydrogen does harm the structural integrity of TMD in question. To ease this problem, simultaneous supply of little chalcogens at a fixed process temperature will help a better control of the doping (see method).

In the last step (Phase III), chalcogen vapor is introduced to repair the lattice and close the reaction. Figure S1 in the Supporting Information shows the result of Se-repaired Cr:WSe_{2-x}, in which most of the V_{Se} were filled, but the ORC reacted region and the intact WSe_2 domain are relatively difficult to distinguish without STEM observation. To label the location where the ORC reaction takes place, we use sulfur to fill the selenium vacancies. By doing this, the sulfurization acts as a reaction indicator, transforming the Cr:WSe_{2-x} into Cr:WS_2 (S + Cr:WSe_{2-x}(s) -> Cr:WS_2(s)). A complete reaction ends up with Cr:WS_2 in the unmasked regions and pristine WSe_2 in the graphene masked regions. Formation of Cr:WS_2 in the unmasked regions indicates that Se vacancies V_{Se} are formed in both top and bottom sublayers of WSe_2 in Phase I. Cr:WSe_{2-x} is an intermediate product in the ORC process and the amount of Se vacancies can be estimated from the sulfurization ratio in the final product of Cr:WS_2. The sulfurization ratio can reach 99% and the difference is significant in comparison with the masked WSe_2 region. The generation of Se vacancies in phase I is the key to dope transition metal atoms. As for the choice of chalcogen atoms for lattice repair, there is no significant difference in the effect of doping. From the sulfurization experiment, we realized that the repairing chalcogen atoms can penetrate to the bottom Se layer, and this may also assist in the interdiffusion of metal atoms.

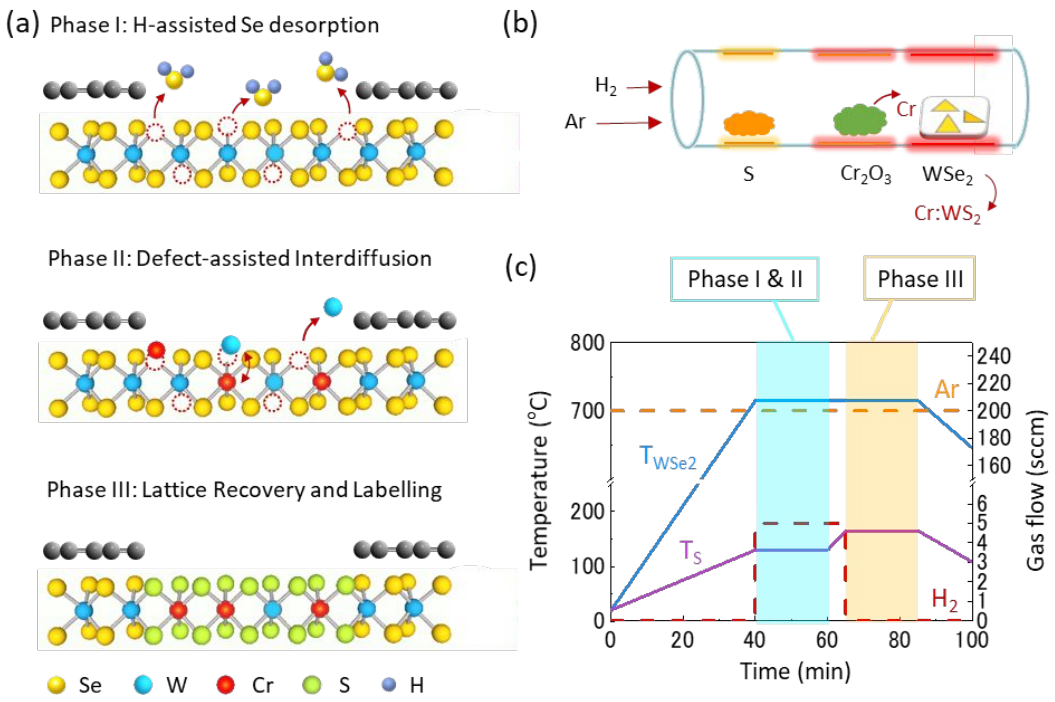

Figure 1. Open-replace-close reaction for area-selective substitution of W sublattice in WSe_2. (a) Schematic illustration of the ORC doping reaction. (b) Schematic of CVD setup for the post-growth Cr doping in WS_2 and WSe_2. (c) Temperature and gas flow rate versus time diagram for the ORC doping of Cr in WSe_2, with the corresponding reaction phases to the reaction time. The blue line shows the temperature-time relations for the ORC reaction at the center of CVD furnace. The purple line is the heating and cooling program for the S source. The orange and red dash lines show the Ar and H_2 gas flows, respectively.

Figure 2a shows the schematics of graphene masking for the ORC substitution reaction. Practically, a periodic array of reaction windows is opened on the mask before stacking on TMD by transfer. Figure 2b and 2c show, respectively, the scanning electron microscopy (SEM) images of partially masked single-layer WSe_2 films before and after the Cr doping. To avoid deposition of amorphous carbon on the sample surface, the SEM images were acquired from control samples lying on a sapphire substrate. The light grey squares correspond to the unmasked WSe_2 regions, whereas the dark grey grid is the WSe_2 covered with single-layer graphene. The graphene mesh shows a high contrast to the

pristine WSe_2 and Cr:WS_2 areas due to the large difference in the number of emitted secondary electrons. Figure 2d shows the atomic resolution STEM annular dark field (ADF) of WSe_2 exposed to H_2 flow before the Cr doping (phase I), in which large amount of Se vacancies are observed and marked by yellow dotted circles. As stated, sulfur was used to fill out the selenium vacancies so as to differentiate the reacted from the non-reacted. For a through reaction, the light grey squares turned into darker contrast (black squares) in the SEM image, indicating a complete transformation of WSe_2 to WS_2 in the unmasked regions. To confirm the success of Cr doping in the unmasked WS_2 region, we performed STEM characterization at the ORC reacted WS_2/WSe_2 interface. Figure 2e shows the ADF image of the interface between Cr:WS_2 and Gr/WSe_2. One can see that the Cr dopants substitute to W sites and exist only in the WS_2 domain with darker contrast (highlighted by purple dotted circles). Note that mixing phases of WSe_{2-x}, WSeS, and Cr:WS_2 will co-exist in the phase II when the sulfurization is not fully complete, and the doping remains localized and non-uniform[22]. In the Gr/WSe_2 domain, one can see Se defects (indicated by yellow dotted circles) remain near the graphene masked edge but no Cr dopants, which probably created during the hydrogen heating process. The difference in the Se defect density between the pristine WSe_2 and the Gr/WSe_2 after the ORC reaction is not significant (Figure S2). In this experiment, a high-quality single-layer graphene was found to be sufficient for masking the doping reaction. Only a weak D peak signal was detected in the Raman spectrum after the reaction (Figure S3, Supporting Information).

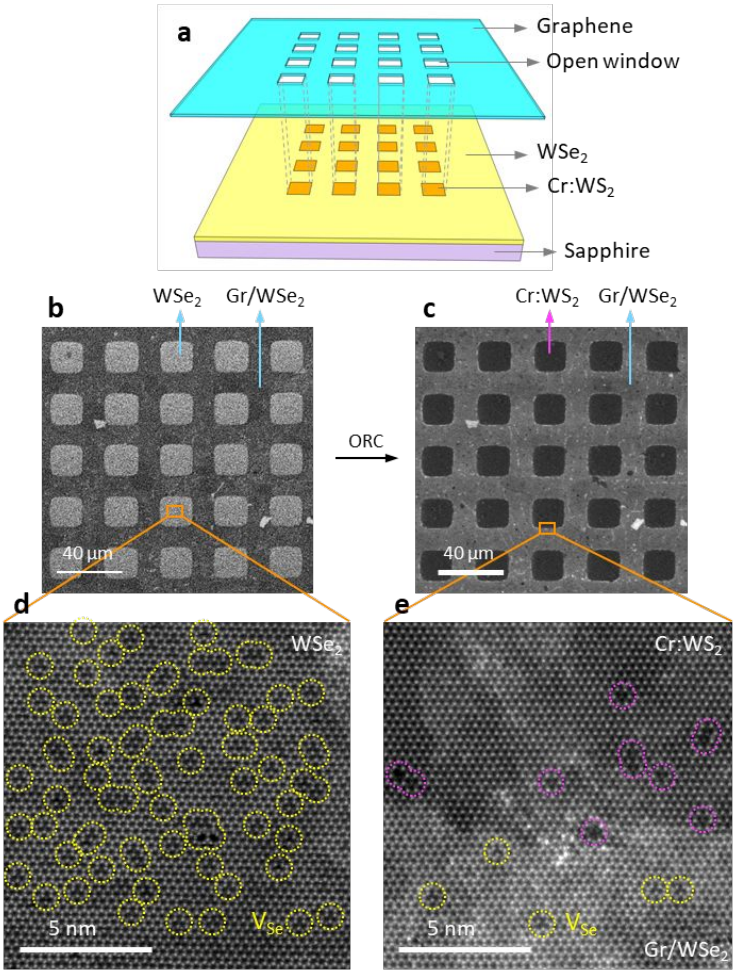

Figure 2. Area-selective doping of Cr in a single-layer WSe_2 film. (a) Schematic of site-selective doping scheme using graphene as a mask. (b) SEM image of the pristine WSe_2 (light grey) film covered by a pre-patterned graphene layer. (c) SEM image of the Cr-doped WSe_2 film in the same area as shown in (b). (d) An ADF image of WSe_2 after 700 °C heating with the aid of hydrogen flow. The Se vacancies are marked with yellow dotted circles. (e) An ADF image of the interface of $Cr:WS_2$ and Gr/WSe_2. Cr dopants are highlighted by purple dotted circles, while Se vacancies are marked by yellow dotted circles.

Evolution of Raman characteristic peaks reveals Cr embedment in the lattice (Figure 3a). For pristine WSe_2 grown by CVD, the most prominent feature in the spectrum appears at 249 cm^{-1} caused by the E^1_{2g} mode.[23,24] Its peak position increased by 4 cm^{-1} as the

doping proceeds, attributed to the co-existence of WSSe and Cr:WS_2. Upon Cr embedment, emergence of characteristic peaks at 176, 352, and 355 cm^{-1} are assigned to the LA(M), 2LA(M), and E^1_{2g} modes of WS_2, respectively. Their intensity increases in proportion to the WS_2/WSe_2 ratio and can be a rough measure of sulfurization level.[25] Two extra peaks located at 379 and 400 cm^{-1} (marked with green triangle and star, respectively) were also found in the spectra. They are characteristic peaks associated with the substitution of W sublattice by other TM dopants, as were also observed in Nb-doped WS_2.[5] A prominent peak at 281 cm^{-1} appears as a result of the sulfurization which forms WSSe structure in some local areas.[26] The E^1_{2g} peak of WSe_2 vanishes in the spectrum when the sulfurization reaction is complete, indicating a macroscopic uniformity of the spatial doping (Figure S4).

Figure 3b shows the evolution of photoluminescence (PL) of WSe_2 with increasing Cr concentration. At the pristine state, the excitonic emission appears at 1.62 eV. Upon Cr embedment, the peak broadens and slightly redshifts, similar to the effect induced by Nb doping in MoS_2 and WS_2.[5,7,27] The broadened peak can be deconvoluted into three subpeaks, attributed to the formation of neutral (1.62 eV), charged (1.56 eV), and bound (1.51 eV) excitons in the host WSe_2. Meanwhile, PL spectrum of Cr:WS_2 develops. The asymmetric profile suggests the coexistence of neutral and charged excitons at different Cr concentrations. The corresponding PL peak of WSSe structure appears between 1.62 and 1.80 eV, varying with the S/Se ratio.[28,29]

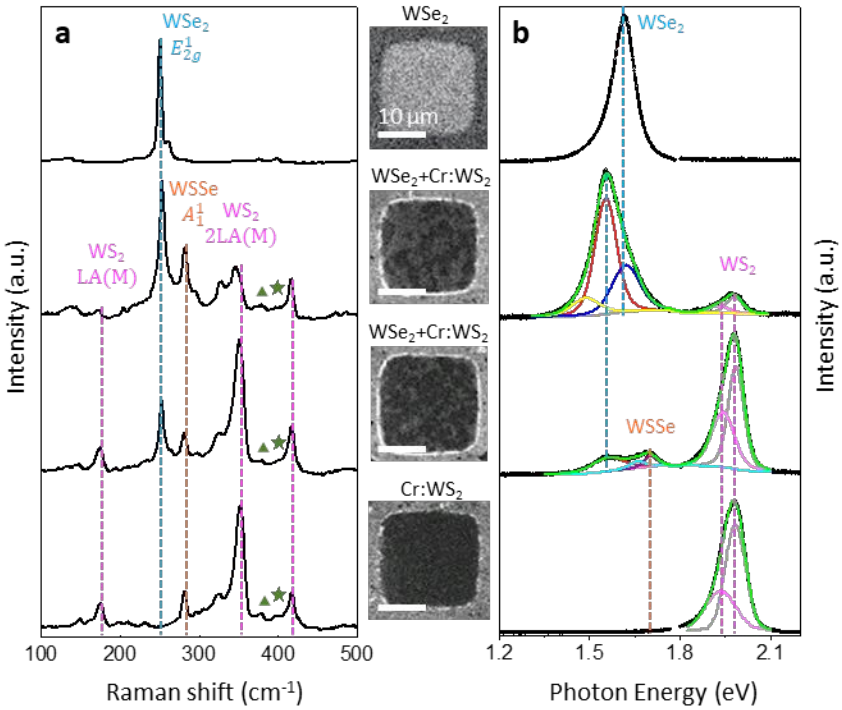

Figure 3. Spectroscopic characterization of WSe_2 and Cr:WS_2 film. (a) Raman spectra of WSe_2 films with different extent of Cr doping. The doped regions are sulfurized and converted to Cr:WS_2 (black). The doping level increases from the top (pristine WSe_2) to the bottom (Cr:WS_2), with corresponding SEM images appended. The SEM images of each grid were acquired from the samples lying on a sapphire substrate. The two green labels indicate the doping-induced characteristic Raman peaks. (b) PL spectra of WSe_2 films with different extent of Cr doping.

To identify the ORC reaction, STEM was used, with single-layer samples suspended in a quantifoil grid and inspected at 60 kV. Figure 4a shows an ADF image of the reacted area. Cr atoms substitute to the W sites and are sandwiched between two S sublayers in an eclipsing configuration. After the ORC process, the trigonal prismatic geometry of the reacted WS_2 regions remains unchanged, preserving the 1H phase after Cr doping. The shown STEM image amounts to a doping density of ~4.9%. Figure 4b shows high-magnification ADF images for Cr dopant in two typical configurations. Most of the Cr atoms appear in an isolated form (enclosed by a yellow dashed triangle), but some of them are coupled at the closest metal sites as a dimerized structure (enclosed by two yellow

dashed triangles). Figure 4c shows a high-magnification ADF image, along with its simulated ADF image in Figure 4d. The Cr atom accounts for a weaker contrast as compared to the W atoms. The experimental ADF intensity profile extracted from the green dotted box in Figure 4c is shown as the dotted curve in Figure 4e, which fits very well to the simulated ADF profile (orange curve) extracted from the orange box in Figure 4d. The Cr substitution is also identified by electron energy loss spectroscopy atom by atom in the selected area. Clear $L_{2,3}$ edges for single Cr dopants were detected and shown in Figure 4f. It should be noted that similar ORC doping can be replicated on WSe_2 monolayer transferred onto a silicon substrate with 300 nm dry oxide atop. Yet, the doping density is found to be generally lower than that of WSe_2 lying on sapphire. This substrate effect is currently unclear and needs further exploration.

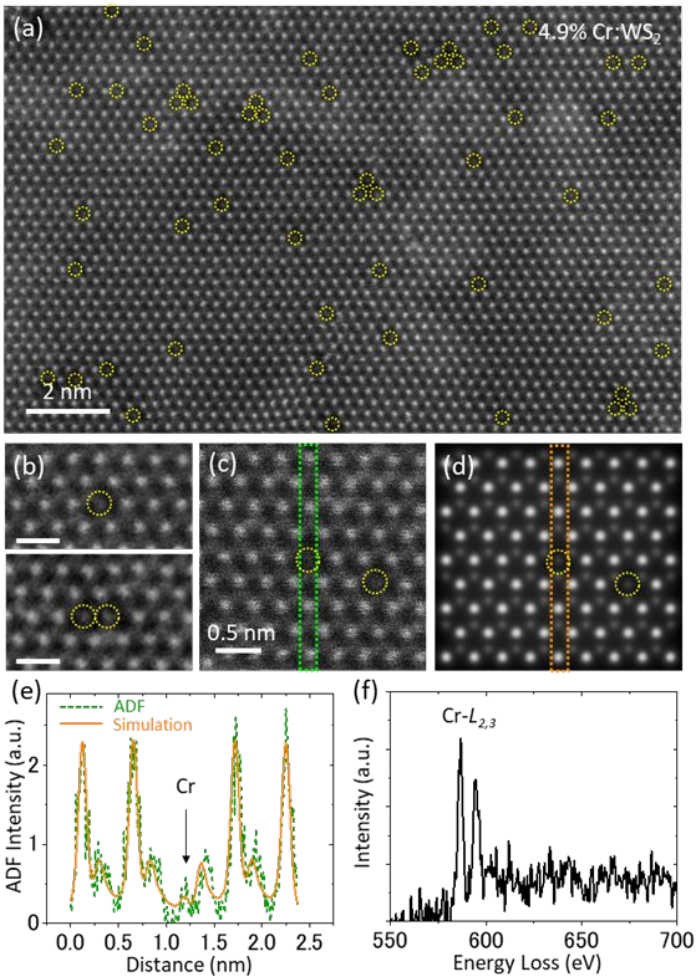

Figure 4. STEM characterization of the unmasked WSe_2 areas after the ORC doping of Cr. The exposed WSe_2 areas has been converted to WS_2 after the reaction. Cr dopants

are marked by yellow dotted circles. (a) An ADF image of WS_2 with high density of Cr dopants, where the dopants appear in dark contrast. (b) High-magnification ADF images of Cr-doped WS_2. The singlet and doublet Cr dopants are enclosed by yellow dashed lines. (c) High-magnification ADF image of Cr-doped WS_2. The green dotted rectangle frames the line scan of intensity profile shown in (e). (d) Simulated ADF image of Cr-doped WS_2, corresponding to the area shown in (c). (e) Intensity comparison between the experimental ADF profile (green dotted curve) and simulated ADF profile (orange curve). (f) Single-atom EELS spectrum of the Cr dopant. The L_3 and L_2 edges are located at 586.5 eV and 594.6 eV, respectively.

Now, we employ the graphene masked ORC reaction on individual WS_2 single crystals. The process starts from CVD-grown WS_2 triangles and ends up with Cr:WS_2 in unmasked regions. Figure 5a shows the SEM image of a selected area, where part of the graphene mask and monolayer WS_2 triangles are included. In the image taken by SEM, secondary electron was detected. We see no distinguishable difference between the masked Gr/WS_2 and doped Cr:WS_2. The surface of the Cr:WS_2 is uniform without extra layer grown on the surface after the ORC process (Figure S5). We used a multiphoton laser scanning microscope to perform a fast imaging of second-harmonic generation (SHG) resonances. The SHG excitation was taken at 1220 and 1260 nm, corresponding to the half excitation energy of 2.03 and 1.97 eV in the SHG process and close to the energy of excitons and trions of WS_2, respectively.[20] Figure 5b shows the SHG images of Gr, Gr/WS_2, and Cr:WS_2 at three different excitation wavelengths. There is no SHG signal in the sapphire area. For Cr:WS_2 excited at 1260 nm, clear SHG enhancement appears as a result of trion resonance. This indicates that the doping of Cr provides excess carriers to facilitate trion formation. In contrast, the SHG image in the Gr/WS_2 region exhibits only a weak but uniform intensity landscape, lacking the contribution of trion. Graphene effectively blocks Cr from doping into the masked WS_2. For the excitonic excitation at 1220 nm, the intensity in Cr:WS_2 is weak, in marked contrast to that in the Gr/WS_2 region. At 840 nm, the SHG intensity is enhanced by the band nesting energy resonance of WS_2,[30] which is far from the quasi-particles' resonance and exhibits a uniform intensity in both Cr:WS_2 and Gr/WS_2. The uniform intensity map excludes the likelihood of strain effect that could affect the

optical response acquired at 1220 and 1260 nm.[31] Note that the slight intensity variation between triangles is attributed to the polarization of the dichroic mirror at 420 nm. For centrosymmetric graphene, no SHG is generally expected. However, at all excitation wavelengths, graphene also produces very weak SHG due to the substrate or doping-induced effect.[32,33]

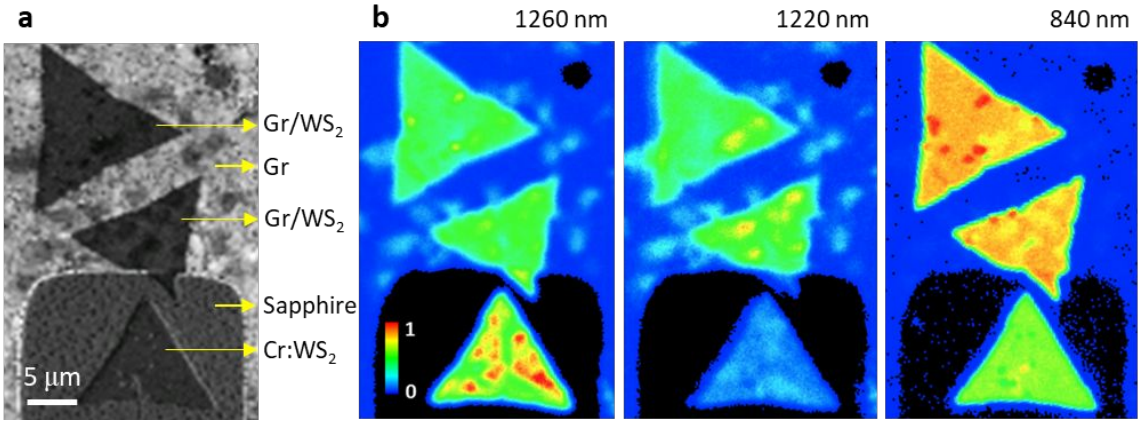

Figure 5. SHG mapping comparison of pristine and Cr-doped WS_2. (a) SEM image of three selected WS_2 single crystals for SHG spatial mapping with the top two covered by graphene and the bottom one exposed for Cr doping. (b) Corresponding SHG images recorded at three different excitation wavelengths. For Gr/WS_2, the SHG image excited at 1260 nm exhibits a uniform intensity and shows no trion contribution. For Cr:WS_2 excited at 1260 nm, clear SHG enhancement appears in the triangular region, which is attributed to the trion resonance. At 1220 nm, there are weak exciton resonances opposite to the trion distribution in Cr:WS_2, but the exciton resonance is relatively uniform in Gr/WS_2. At 840 nm, the SHG intensity is enhanced by the band nesting energy resonance, but exhibits a uniform intensity in both Cr:WS_2 and Gr/WS_2. At all excitation wavelengths, Gr also produces very weak SHG. Intensity is shown with a rainbow color scale.

The doping effect of the substitutional Cr atoms in WS_2 was measured by scanning photoelectron microscopy (SPEM) and μ-XPS. In the SPEM mode, combining with the sub-micrometer soft x-ray beam and piezo motor stage, the core-level photoelectrons can be collected by the analyzer during the scanning process. The signal intensity from a specific core level can be translated into spatial distribution of the object in question, with the localized chemical state information conveyed from the SPEM image. Figure 6a shows the SEM image of a WS_2 single crystal which is partially covered by a graphene mesh. The binding energy of 32.5~33.5 and 284.0~285.0 eV is, respectively, selected for the chemical mapping of W $4f_{7/2}$ and C 1*s* levels. The photon energy was calibrated by the Au $4f_{7/2}$ core level line with binding energy of 84.0 eV, emitted from a clean Au foil electrically contacted with the samples[34,35]. The WS_2 triangle (yellow) and graphene mesh (cyan) can be clearly distinguished from the SPEM images, as shown in Figure 6b and 6c. The SPEM also provides high energy resolution μ-XPS mode to acquire core-level photoelectron spectra (Figure 6d). To distinguish the doping effect of masked and unmasked regions, peak deconvolution of the two areas is performed for both W 4*f* and S 2*p* lines. The peak area in yellow and cyan corresponds to the Gr/WS_2 and Cr:WS_2, respectively. Both of the W 4*f* and S 2*p* binding energies show an energy shift of 0.25 eV between the masked and unmasked regions. The redshift of binding energy in the unmasked area indicates that the Fermi level moves closer toward the valence band maximum of Cr:WS_2,[36] manifesting an *p*-type doping effect caused by the substitutional Cr atoms. Notably, the full width at half maximum (FWHM) of the W 4*f* and S 2*p* core levels remains the same for the masked and unmasked regions, indicating the similar chemical environment for the pristine WS_2 and Cr:WS_2, i.e., the ORC embedment reaction does not create extra traceable amount of lattice defects like S vacancies.

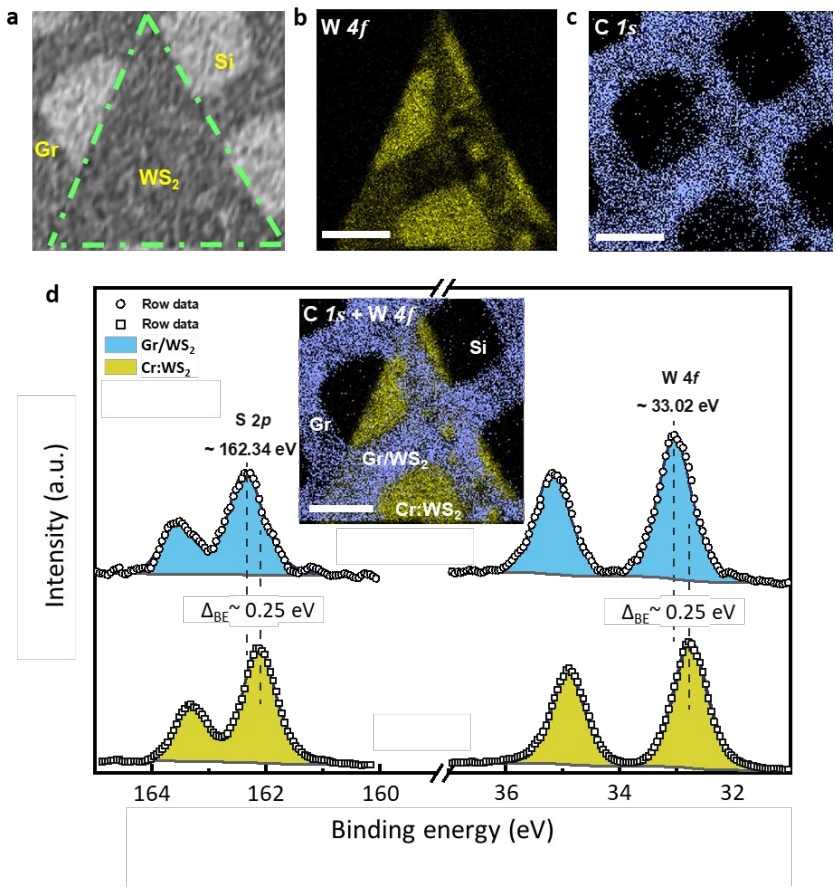

Figure 6. SPEM and μ-XPS characterization of pristine and Cr-doped WS_2. (a) SEM image of a WS_2 single crystal covered by a pre-patterned graphene mask. (b) SPEM spatial mapping of the W 4*f*. (c) SPEM spatial mapping of the C 1*s*. (d) μ-XPS spectra of W 4*f* and S 2*p* taken from the Gr/WS_2 (circles) and $Cr:WS_2$ (squares) areas. Cyan and dark yellow areas in the spectra are the fitting for Gr/WS_2 and $Cr:WS_2$, respectively. The inset shows the SPEM chemical mapping image combined from (b) and (c). The scale bars in the figures are all 10 μm.

Using the ORC method, the doping concentration can be varied by the reaction time (see Figure 7a-7c for $Cr:WS_2$ and Figure S6 for $Cr:WSe_2$). Previous study suggests that the doping behavior is dominated by the kinetic chalcogen defect distribution, and the TM atoms should be easier to dope into W positions when chalcogen vacancies are present.[22] In the ORC process, the existence of chalcogen vacancies created in the first step of the synthesis process is the key point to dope foreign TM atoms at W site. Therefore, we can

adjust the concentration of Cr dopants by controlling the surface Se deficiencies in the first heating process. The highest doping concentration in our experiment is about 7%. Before reaching the solubility limit, the concentration varies linearly with time, showing a constant doping rate at a fixed reaction temperature (Figure 7d). The W atoms will lose bonding or become less stable when the surrounding Se vacancies are created. At such moment, the foreign transition metals can have chance to replace the W atoms. The replaced W atoms can replace the Cr dopants again or diffuse to fill another W vacancies or be carried away by the flowing gas. It is impossible to covert WSe_2 into $CrSe_2$ by CVD method with a flux of Cr source. The formation energy of $CrSe_2$ is -0.196 eV/atom, while the formation energy of WSe_2 is -0.558 eV/atom which is much lower than $CrSe_2$. Besides, ORC method can also be used for doping desired TM atoms at the selected areas. We demonstrated the doping with Mo, V, and Fe into individual WS_2 specimens as shown in the Figure 7e-7g. The dopants can be distinguished from the W atoms according to the ADF intensity. Atom-by-atom EELS analyses confirm the substitutional doping elements as shown in Figure 7h-7j. The doping scheme is also applicable to different types of TMDCs, since they share the same structure with transition metal layer sandwiched by two chalcogen layers. Nevertheless, Se-based TMDCs are easier than S-based TMDCs to proceed transition metal substitution because Se is readily to sublime at an elevated temperature, leaving Se vacancies for the incorporation of foreign impurities. For example, the same doping approach applying on WS_2 will result in a much lower doping concentration. Our doping method can also be used to form a lateral heterostructure. An example is to form a WSe_2/MoS_2 heterojunction. Figure S7 in the Supporting Information shows the schematic of forming such a heterostructures. Raman analysis before and after the ORC reaction is, respectively, shown in Figure S8 and S9 (Supporting Information). The patterned graphene mask can further be removed by an oxygen plasma etching, but it may generate massive defects in the underlying TMD materials if no optimal recipe for a clear etching stop between these two materials is found. From the perspective of applications, hexagonal boron nitride (h-BN) should be a better mask for the ORC doping. With using the ORC method, one could easily design the doping areas and the types of dopants for further applications in electronic devices, photodetectors, and sensors.

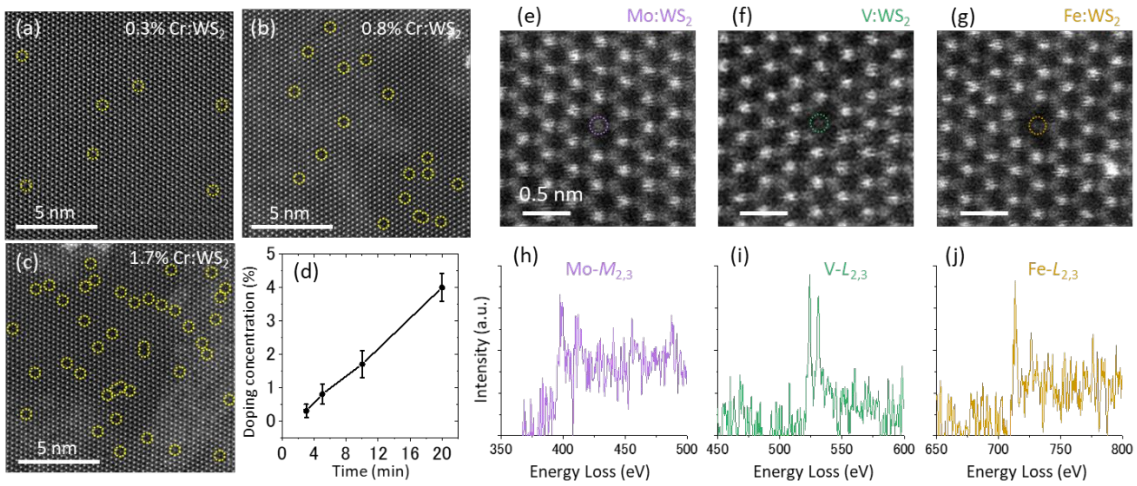

Figure 7. Controllable doping by ORC method. (a-c) ADF images of Cr-doped WS_2 with different doping concentration. The Cr dopants are marked by yellow dotted circles. (d) Cr doping rate in WS_2. (e-g) ADF images of introducing different dopants of Mo, V, and Fe in WS_2 lattice by using ORC method. The Mo, V, and Fe dopants are marked by purple, green and khaki dotted circles. (h-j) The corresponding EEL spectra of the Mo:WS_2, V:WS_2, and Fe:WS_2, respectively.

Conclusions

In conclusions, we demonstrate a site-selective doping scheme for single-layer TMD materials, in which WS_2 is covered by pre-patterned graphene as a mask and substitutionally doped by Cr in the unmasked areas. Instead of graphene, CVD grown hexagonal boron nitride should be also a great candidate as the ORC mask. This doping approach allows local modification of the host TMD semiconductors for desired electrical, excitonic, magnetic, and catalytic properties. The core technology of this doping scheme lies in the control of chalcogen sublimation in a devised CVD process during which dopant impurities can be embedded and substitute the transition metal sublattice through the massive numbers of surface vacancies. After the doping reaction, the surface vacancies can be filled out by sulfurization or selenization, providing another degree of freedom to vary the local crystalline structure. This will meet the demand for the quest of both *n*- and *p*-channel transistors in the future integrated circuits based on such a layered semiconductor.

Methods

Patterning graphene mask

Large area single-layer graphene was grown on Cu foil using standard CVD process.[37,38] The single-layer graphene coverage rate is over 99%. The as grown graphene layer was transferred onto SiO_2/Si surface. Note that a clean wet transfer process reported previously is used throughout the whole experiments for the graphene or TMD film transfer.[39] Then, the graphene surface was spin-coated with a layer of PMMA and an array of square windows was created by an e-beam lithography and reactive ion etching. Oxygen plasma was performed to the patterned PMMA/graphene for 10 sec to remove the exposed graphene at the patterned square windows. Then, the patterned graphene was further transferred onto the WSe_2 film grown on sapphire for the ORC doping.

ORC doping

Site-selective Cr doping in WSe_2 and WS_2 was carried out in a 3-inch homemade CVD furnace. Monolayer WSe_2 or WS_2 samples were placed in the centre of CVD furnace. The doping source, chromium oxide (50 mg), was placed in a quartz boat and located at the upstream side of the sample for ~3 cm. The sulfur powder (300 mg) was placed at the upstream side of the furnace at carefully adjusted location in order to set the temperature. The temperature of the furnace was risen and kept at 715 °C through the whole reaction process. The sulfur position was heated by an induction heater to 130 °C in order to provide little chalcogens to maintain the structural integrity in phase I and phase II. Then the sulfur temperature was ramped up to 160~170 °C to increase the chalcogen vapor to repair the lattice in phase III. The growth time depends on the desired doping concentration, during which argon (200 sccm) was constantly flowing through the tube under 20 Torr working pressure. After the growth, the working pressure was risen to 25.6 torr, and then the furnace was cooled down to room temperature naturally with argon flowing constantly.

STEM characterization

After the ORC doping process, the entire graphene/Cr-doped WSe_2 was again spin coated with polycarbonate. The sample was detached from the sapphire substrate in diluted HF and transferred to the TEM grid through a clean-transfer technique reported previously.[40] STEM images were acquired by using JEOL ARM based microscope equipped with JEOL delta corrector and a cold field emission gun operating at 60 kV. The probe current is set at 30 pA. The convergence semi-angle and the inner acquisition semi-angle are 37 and 76 mrad for STEM imaging, respectively. The EELS core loss spectra were taken by using Gatan Rio CMOS camera specially designed for low-voltage spectroscopy. The single atom EELS was performed by line scan with 0.2 sec/pixel for 50 steps. The STEM image simulation was conducted by using MacTempas software.

SPEM and μ-XPS

SPEM and μ-XPS measurements were performed at Taiwan Light Source (TLS) 09A1 beamline of the National Synchrotron Radiation Research Center (NSRRC), Taiwan. Through the combination of the Fresnel zone plate optics and synchrotron x-ray, the focusing technique enables XPS measurement with a spatial resolution of approximately 100nm. The photoelectron energy analyzer (model 10–360, PHI) equipped with 16-channel electron collector, core level electron can be collected in the 16 channels during the scanning. Thus, the localized chemical information can be obtained from the image. The incident x-ray (photon energy 400 eV) is normal to the sample surface, and the analyzer is located at a specific angle of 54° from the x-ray incident direction. The geometry allows lateral heterostructure characterization by the surface sensitive measurement. The photon energy was calibrated by the Au $4f_{7/2}$ core level line with binding energy of 84.00eV, emitted from a clean Au foil electrically contacted with the samples. All the measurements were carried out at room temperature. Combining the surface sensitive capability and submicrometer spatial resolution, SPEM is an ideal tool to study the electronical and chemical structures of 2D materials.[35,36]

SHG measurements

SHG measurements were performed using an in-house multiphoton laser scanning microscope. The fundamental laser field was provided by a mode-locked Ti:sapphire laser

and an optical parametric oscillator with a pulse width of 140~200 fs and a repetition rate of 80 MHz. The laser pulse of 1260 nm was focused to a spot size of ~1.9 μm on the sample by a 20×0.8NA plan apochromat objective. The lateral resolution is ~0.6 μm. The backscattered second-harmonic emission generated from the WS_2 monolayers passed through a short-pass dichroic mirror and was divided into four channels using three dichroic mirrors and one mirror was detected using photomultiplier tubes.

Optical characterizations

We characterize the TMD samples on sapphire before and after ORC doping reaction using confocal Raman (Thermo scientific, DXR) and micro-PL (Horiba spectrometer, iHR 550). An excitation laser wavelength of 532 nm with a laser power below 0.1 mW was used to acquire the Raman active modes and PL spectra, so as to avoid laser-induced heating and damage. The light spot at the focal plane is close to the diffraction-limited size of 500 nm in diameter under a 100 × objective lens (NA = 0.9).

Supporting Information

The supporting information is available free of charge at:

Additional STEM-EELS study of Cr doped WSe_2 after ORC reaction. STEM images of WSe2 before and after ORC reaction for Se defect comparison. Raman spectra of the patterned graphene mask after ORC reaction. Raman and PL mapping and AFM image of Cr:WS_2. STEM images of doping Cr in WSe_2 with different doping concentration. Fabrication and Raman characterization of MoS_2-stripe/Wse_2 lateral heterostructure by using ORC reaction method.

Acknowledgement

We thank the Ministry of Science and Technology (MOST) Taiwan Grants MOST 109-2124-M-007-002-MY3, MOST 109-2112-M-007-027-MY3, MOST 106-2628-M-007-003-MY3, and MOST 109-2124-M-006-001 as well as Academia Sinica (AS) Grant AS-TP-106-A07. Y.-C.L. and K.S. acknowledge to the JSPS-KAKENHI (JP16H06333, JP18K14119, JP21H05235, and JP22H05478), JST-CREST program (JPMJCR20B1,

JMJCR20B5, JPMJCR1993), the ER-C "MORE-TEM" Project, JSPS A3 Foresight Program, and Kazato Research Encouragement Prize.

References

1 Y. C. Lin, R. Torsi, D. B. Geohegan, J. A. Robinson and K. Xiao, *Adv. Sci.*, 2021, **2004249**, 1–26.

2 M. Ghorbani-Asl, S. Kretschmer, D. E. Spearot and A. V. Krasheninnikov, *2D Mater.*, 2017, **4**, 025078.

3 S. Bertolazzi, S. Bonacchi, G. Nan, A. Pershin, D. Beljonne and P. Samorì, *Adv. Mater.*, 2017, **29**, 1606760.

4 T. Shi, R. C. Walker, I. Jovanovic and J. A. Robinson, *Sci. Rep.*, 2017, **7**, 4151.

5 Z. Qin, L. Loh, J. Wang, X. Xu, Q. Zhang, B. Haas, C. Alvarez, H. Okuno, J. Z. Yong, T. Schultz, N. Koch, J. Dan, S. J. Pennycook, D. Zeng, M. Bosman and G. Eda, *ACS Nano*, 2019, **13**, 10768–10775.

6 V. Kochat, A. Apte, J. A. Hachtel, H. Kumazoe, A. Krishnamoorthy, S. Susarla, J. C. Idrobo, F. Shimojo, P. Vashishta, R. Kalia, A. Nakano, C. S. Tiwary and P. M. Ajayan, *Adv. Mater.*, 2017, **29**, 1703754.

7 M. E. Pam, J. Hu, Y. S. Ang, S. Huang, D. Kong, Y. Shi, X. Zhao, D. Geng, S. J. Pennycook, L. K. Ang and H. Y. Yang, *ACS Appl. Mater. Interfaces*, 2019, **11**, 34862–34868.

8 S. Z. Yang, Y. Gong, P. Manchanda, Y. Y. Zhang, G. Ye, S. Chen, L. Song, S. T. Pantelides, P. M. Ajayan, M. F. Chisholm and W. Zhou, *Adv. Mater.*, 2018, **30**, 1803477.

9 H. Li, J. K. Huang, Y. Shi and L. J. Li, *Adv. Mater. Interfaces*, 2019, **6**, 1900220.

10 Y. Zhang, Y. Yao, M. G. Sendeku, L. Yin, X. Zhan, F. Wang, Z. Wang and J. He, *Adv. Mater.*, 2019, **31**, 1901694.

11 L. Loh, Z. Zhang, M. Bosman and G. Eda, *Nano Res.*, 2021, **14**, 1668–1681.

12 H. Cai, Y. Yu, Y. C. Lin, A. A. Puretzky, D. B. Geohegan and K. Xiao, *Nano Res.*, 2021, **14**, 1625–1649.

13 M. G. Stanford, P. D. Rack and D. Jariwala, *npj 2D Mater. Appl.*, 2018, **2**, 20.

14 M. Mahjouri-Samani, M. W. Lin, K. Wang, A. R. Lupini, J. Lee, L. Basile, A. Boulesbaa, C. M. Rouleau, A. A. Puretzky, I. N. Ivanov, K. Xiao, M. Yoon and D. B. Geohegan, *Nat. Commun.*, 2015, **6**, 7749.

15 G. Kim and H. S. Shin, *Nanoscale*, 2020, **12**, 5286–5292.

16 K. Suenaga, H. G. Ji, Y.-C. Lin, T. Vincent, M. Maruyama, A. S. Aji, Y. Shiratsuchi, D. Ding, K. Kawahara, S. Okada, V. Panchal, O. Kazakova, H. Hibino, K. Suenaga and H. Ago, *ACS Nano*, 2018, **12**, 10032–10044.

17 C.-H. Yeh, Z.-Y. Liang, Y.-C. Lin, H.-C. Chen, T. Fan, C.-H. Ma, Y.-H. Chu, K. Suenaga and P.-W. Chiu, *ACS Nano*, 2020, **14**, 985–992.

18 J. D. McBrayer, R. M. Swanson and T. W. Sigmon, *J. Electrochem. Soc.*, 1986, **133**, 1242–1246.

19 C. H. Yeh, Z. Y. Liang, Y. C. Lin, H. C. Chen, T. Fan, C. H. Ma, Y. H. Chu, K. Suenaga and P. W. Chiu, *ACS Nano*, 2020, **14**, 985–992.

20 T. H. Tsai, Z. Y. Liang, Y. C. Lin, C. C. Wang, K. I. Lin, K. Suenaga and P. W. Chiu, *ACS Nano*, 2020, **14**, 4559–4566.

21 C. H. Ho, W. H. Chen, K. K. Tiong, K. Y. Lee, A. Gloter, A. Zobelli, O. Stephan and L. H. G. Tizei, *ACS Nano*, 2017, **11**, 11162–11168.

22 Y.-C. Lin, J. Karthikeyan, Y.-P. Chang, S. Li, S. Kretschmer, H.-P. Komsa, P.-W. Chiu, A. V. Krasheninnikov and K. Suenaga, *Adv. Mater.*, 2021, **2007819**, 1–8.

23 C.-H. Yeh, Z.-Y. Liang, Y.-C. Lin, H.-C. Chen, T. Fan, C.-H. Ma, Y.-H. Chu, K. Suenaga and P.-W. Chiu, *ACS Nano*, 2020, **14**, 985–992.

24 X. Zhang, X. F. Qiao, W. Shi, J. Bin Wu, D. S. Jiang and P. H. Tan, *Chem. Soc. Rev.*, 2015, **44**, 2757–2785.

25 R. J. Chang, Y. Sheng, G. H. Ryu, N. Mkhize, T. Chen, Y. Lu, J. Chen, J. K. Lee, H. Bhaskaran and J. H. Warner, *ACS Appl. Mater. Interfaces*, 2019, **11**, 24279–24288.

26 M. M. Petrić, M. Kremser, M. Barbone, Y. Qin, Y. Sayyad, Y. Shen, S. Tongay, J. J. Finley, A. R. Botello-Méndez and K. Müller, *Phys. Rev. B*, 2021, **103**, 035414.

27 J. Suh, T. L. Tan, W. Zhao, J. Park, D. Y. Lin, T. E. Park, J. Kim, C. Jin, N. Saigal, S. Ghosh, Z. M. Wong, Y. Chen, F. Wang, W. Walukiewicz, G. Eda and J. Wu, *Nat. Commun.*, 2018, **9**, 199.

28 X. Duan, C. Wang, Z. Fan, G. Hao, L. Kou, U. Halim, H. Li, X. Wu, Y. Wang, J. Jiang, A. Pan, Y. Huang, R. Yu and X. Duan, *Nano Lett.*, 2016, **16**, 264–269.

29 K. KY, L. S, P. K, K. Y, W. WJ, K. D, S. JG, P. J, K. JH, L. Z and K. H, *ACS Appl Mater Interfaces*, 2018, **10**, 34163–34171.

30 D. Kozawa, R. Kumar, A. Carvalho, K. Kumar Amara, W. Zhao, S. Wang, M. Toh, R. M. Ribeiro, A. H. Castro Neto, K. Matsuda and G. Eda, *Nat. Commun.*, 2014, **5**, 4543.

31 L. Mennel, M. M. Furchi, S. Wachter, M. Paur, D. K. Polyushkin and T. Mueller, *Nat. Commun.*, 2018, **9**, 516.

32 Y. Zhang, D. Huang, Y. Shan, T. Jiang, Z. Zhang, K. Liu, L. Shi, J. Cheng, J. E. Sipe, W. T. Liu and S. Wu, *Phys. Rev. Lett.*, 2019, **122**, 47401.

33 M. Vandelli, M. I. Katsnelson and E. A. Stepanov, *Phys. Rev. B*, 2019, **99**, 165432.

34 S. Cho, S. Kim, J. H. Kim, J. Zhao, J. Seok, D. H. Keum, J. Baik, D. Choe, K. J. Chang, K. Suenaga, S. W. Kim, Y. H. Lee and H. Yang, *Science*, 2015, **349**, 625–628.

35 M. H. Chiu, C. Zhang, H. W. Shiu, C. P. Chuu, C. H. Chen, C. Y. S. Chang, C. H. Chen, M. Y. Chou, C. K. Shih and L. J. Li, *Nat. Commun.*, 2015, **6**, 7666.

36 J. W. Chen, S. T. Lo, S. C. Ho, S. S. Wong, T. H. Y. Vu, X. Q. Zhang, Y. De Liu, Y. Y. Chiou, Y. X. Chen, J. C. Yang, Y. C. Chen, Y. H. Chu, Y. H. Lee, C. J. Chung, T. M. Chen, C. H. Chen and C. L. Wu, *Nat. Commun.*, 2018, **9**, 3143.

37 C. C. Lu, Y. C. Lin, C. H. Yeh, J. C. Huang and P. W. Chiu, *ACS Nano*, 2012, **6**, 4469–4474.

38 C. H. Yeh, Y. W. Lain, Y. C. Chiu, C. H. Liao, D. R. Moyano, S. S. H. Hsu and P. W. Chiu, *ACS Nano*, 2014, **8**, 7663–7670.

39 Y. C. Lin, C. Jin, J. C. Lee, S. F. Jen, K. Suenaga and P. W. Chiu, *ACS Nano*, 2011, **5**, 2362–2368.

40 Y. C. Lin, C. C. Lu, C. H. Yeh, C. Jin, K. Suenaga and P. W. Chiu, *Nano Lett.*, 2012, **12**, 414–419.